A Confinement-Driven Nucleation Mechanism of Metal Oxide Nanoparticles Obtained via Thermal Decomposition in Organic Media

Geoffrey Cotin, Benoît Heinrich, Francis Perton, Céline Kiefer, Gregory Francius, Damien Mertz, Barbara Freis, Benoit Pichon, Jean-marc Strub, Sarah Cianférani, et al.

A confinement driven nucleation mechanism of metal oxide nanoparticles obtained via thermal decomposition in organic media

Geoffrey Cotin[1,2], Benoît Heinrich[1], Francis Perton[1,2], Céline Kiefer[1,2], Gregory Francius[3], Damien Mertz[1,2], Barbara Freis[1], Benoit Pichon[1,2], Jean-Marc Strub[4], Sarah Cianférani[4], Nathalie Ortiz Peña[1], Dris Ihiawakrim[1], David Portehault[6], Ovidiu Ersen[1,2,] Amir Khammari[1], Matthieu Picher[1], Florian Banhart[1], Clement Sanchez[5,6], Sylvie Begin-Colin[1,2*]

[1] Université de Strasbourg, CNRS, Institut de Physique et Chimie des Matériaux de Strasbourg, UMR 7504, F-67034 Strasbourg, France

[2] Labex CSC, Fondation IcFRC/Université de Strasbourg, 8 allée Gaspard Monge BP 70028 F - 67083 Strasbourg Cedex.

[3] Université de Lorraine and CNRS. LPCME UMR 7564, F-54000 Nancy, France

[4] Université Strasbourg, CNRS, IPHC, Laboratoire de Spectrométrie de Masse BioOrganique, UMR 7178, F-67000 Strasbourg, France

[5] USIAS Chair of Chemistry of ultradivided matter, University of Strasbourg Institut of Advanced Study, 67000, Strasbourg France

[6-]Sorbonne Université, CNRS UMR 7574, Collège de France, LCMCP, 4 place Jussieu 75252 Paris cedex 05, France

ABSTRACT

Thermal decomposition is a very efficient synthesis strategy to obtain nanosized metal oxides with controlled structures and properties. In particular, for iron oxide nanoparticles synthesis, it allows an easy tuning of the nanoparticle's size, shape and composition. This structural and size control is often explained by the LaMer theory involving a clear separation between the nucleation and growth steps. In the present work, the events before the nucleation of iron oxide nanocrystals were investigated by combining different complementary *in situ* characterization techniques (liquid-cell TEM, high-temperature TEM, SAXS/WAXS). These characterisation experiments were carried on not only on powdered iron stearate precursors with a well-known composition and structure but also on a preheated liquid reaction mixture. This study revealed a new nucleation mechanism for the thermal decomposition method: instead of a homogeneous nucleation within the solvent, the nucleation occurs within vesicle-like "nanoreactors" which confine the reactants. The different observed steps are: (1) the melting and coalescence of iron stearate particles, leading to "droplet-shaped nanostructures" which act as nanoreactors; (2) the formation of a hitherto unobserved crystalline phase of iron stearate within the nucleation temperature range of 200-280°C, simultaneaously with the loss of stearate chains and the Fe(III) to Fe(II) reduction; (3) the formation of iron oxide nuclei inside the nanoreactors, which are then ejected from these nanoreactors. This mechanism, observed here for the first time, paves the way towards a better mastering of the synthesis process of metal oxide based nanoparticles and the control of their properties.

INTRODUCTION

Various iron oxide nanoparticles (IONPs) synthesis methods have been set up among years but currently one of the most adapted one allowing fine control over the structural parameters of NPs is the heated-up thermal decomposition (TD)[1–3]. Indeed, the IONPs characteristics, which need to be tuned to the targeted properties and applications (magnetism, nanomedicine, catalysis…), are mainly tuned by controlling their size, shape and composition, which is quite easy by using this TD method. The TD method developed by Hyeon et al[1,2,4] consists in the decomposition of an iron precursor in a high boiling point organic solvent in presence of one surfactant, which ensure grain growth control and colloidal stability. Spherical IONPs with a controlled mean size and a narrow size distribution were thus elaborated and different NP shapes were obtained by tuning the heating rate and using shape driving ligands, which will adsorb on specific faces of nuclei and thus promote the growth of other faces driving thus specific shapes.[5,6],[7,8] IONPs with different sizes and shapes have been thus widely synthesized using this method.

Such versatility in tuning NPs characteristics is often related to the TD process itself, which is reported to ensure a clear separation between nucleation and growth steps, which is the key factor for obtaining NPs with a narrow size distribution and also tailored specifications. Indeed, the stages between the beginning of precursor TD and the NPs formation are currently described by the nucleation and growth theory reported by LaMer et Dinegar[9] in 1950. Three major stages are proposed (Figure 1): i) iron based monomers generation (monomers are reported to result from the precursor decomposition upon increasing temperature[4]) ; ii) nucleation after which a critical nucleation concentration (C_{min}^{nu}) in monomer is reached and iii) then growth of nuclei after which the monomer concentration goes below $C_{min}^{nu}$and stays above the saturation C_s. Therefore, nuclei are generated during the nucleation step that is followed by a homogeneous growth step without the creation of new nuclei [4,10,11]. Such LaMer theory allows thus explaining the NPs synthesis with narrow size distribution and the possibility to obtain different shape using shape driving ligands. The TD synthesis with its variety of experimental parameters such as temperature, reaction time, concentration and nature of precursor, surfactants and solvent… offers a proper freedom towards the design of NPs (e.g. to tune the size, morphology and composition). However, because of these numerous parameters, there is always some lack in the IONPs synthesis control and reproducibility, which currently limit their development, and make them harder to scale up, which is a prerequisite for their further use in industry.

The nucleation has been proved, by using different characterization techniques, to occur in the range 200-300°C and more precisely around 280 °C for iron carboxylate complexes such as iron oleate and iron stearates [2,4,10,12–15]. Though research works converge on the same temperature range in which the nucleation takes place, the intrinsic TD mechanism still remains unravelled and in particular the structure and composition of monomer generated by the decomposition of the precursor. Most interesting studies rely on *ex-situ* analysis of samples extracted from the synthesis media at different reaction times. *E.g.* Kwon et al.[4]

studied the TD of iron oleate in octadecene or eicosene by performing magnetic measurements, size exclusion chromatography and TEM-based analyses. They have been able to identify the temperature range of nucleation in their system but most importantly, they reported that intermediates species, consisting in poly-oxo iron complexes named monomers, are formed before the nucleation step. More recently, Lassenberger and al[16] studied the *in-situ* NPs formation with Small Angle X-ray Scattering (SAXS). They have decomposed iron pentacarbonyl $Fe(CO)_5$ with oleic acid (OA) in dioctylether and were able to show that the synthesis mechanism takes place in several stages. First, an iron oleate is formed from the reaction of the precursor with OA, then structures that are not crystallized NPs are observed before the burst of nucleation and then growth step. These structures were ascribed to the polyiron oxo species reported by Kwon et al.[4] but they suggested that it could be micellar structure of OA encapsulated precursor. In fact, the stages before nucleation are quite complex to analyze using standard characterization techniques.

In that challenging context, with the aim to get a better insight in the TD mechanism, we investigated the early and different stages up to the nucleation step of the TD process by combining different *in situ* characterization techniques. The iron precursor is an iron stearate with a composition 1Fe:2St (one iron atom for two stearate (St) chains named $FeSt_2$) synthesized "in house" by coprecipitation in water[12,13,17]. The composition and structure of this iron stearate $FeSt_2$ was studied and it consists of a lamellar compound composed mainly of the polynuclear complex $[Fe_3(\mu_3\text{-}O)St_6.xH_2O]Cl$ [17]. The iron polycations are organized in planes separated by perpendicular stearate chains in all trans configuration (Figure 2). The reproducible synthesis of 10 nm sized NPs has been demonstrated with this precursor[12]. Recent investigations confirmed the reported hypotheses that the nuclei, in such reaction media with iron carboxylate precursor, display a wüstite composition[13]. They suggested also a nucleation mechanism based on the condensation of these polynuclear complexes after their catalytic decarboxylation occuring simultaneously with reduction of Fe(III) in Fe(II) [13,17,18]. In this present work, we investigated the stages leading to the nuclei formation. We have considered $FeSt_2$ and also heat-treated $FeSt_2$ (at 140°C for 48h), named $FeSt_{2d}$, because they led to the same NPs size in the standard 10 nm NPs synthesis conditions (Figure S1). Worthy to note that $FeSt_{2d}$ showed a slightly faster reaction and NPs with anisotropic shape were easier to obtain[6,12]. In fact, by contrast with $FeSt_2$, $FeSt_{2d}$ is composed of a mixture of $[Fe_3(\mu_3\text{-}O)St_6.xH_2O]St$ and $[Fe_7(\mu_3\text{-}O(H))_6(\mu_2\text{-}O(H))_xSt_{12-x}]St$) polynuclear complexes (details in SI part, Figures S2-4).

The TD mechanism of these iron stearates up to the nucleation step has been analyzed in depth by combining several fine and powerfull characterization techniques such as liquid-phase TEM, in-situ TEM at high temperature, atomic force microscopy (AFM) in organic liquid, small and wide-angle X-ray scattering (SWAXS) of powdered samples and small-angle X-ray scattering (SAXS) of reaction solutions. SAXS and SWAXS techniques were used because metal stearates are long chain carboxylate compounds, which are well known to exhibit a liquid crystal behavior[19–23] and the effect of this behavior needs to be studied. Thermogravimetric analyses (TGA) on iron precursors were shown very suitable to establish the temperature

ranges of the nucleation and growth steps and thus, TEM at high temperature on iron stearate powders provided useful information on the evolution of iron stearate particles up to the nucleation step. Liquid-cell TEM[24–28] has already been used in the fields of electrocatalysis[29] and energy storage as well as for investigating biological cells[24] and nanomaterials synthesis[30–32]. However one may notice that studies on NPs synthesis mechanisms deal mainly with the growth process of metallic or bimetallic or core-shell NPs (Cu, Pd, Pt, Au, Au-Pd, Fe_3Pt...)[33]. With iron oxide NPs in particular, the colloidal stability of iron oxide NPs, their aggregation mechanisms leading to nanorods or the growth step of iron oxide NPs have been reported but nothing the type of monomers and on the stages before the formation of nuclei to the best of our knowledge[25,32,34–37]. It is often reported that there is no temperature increase during liquid cell TEM (LCTEM) and rather radiolysis reactions involving mostly water. The radiolysis of water generates radicals inducing reducting or oxydating reactions in the liquid phase[25,38,39]. The electron beam was also reported to favor the reduction of ions. In our specific case, LCTEM is thus expected to favor the reduction of Fe^{3+} bound to carboxylate groups: it would thus simulate suitably the effect of the temperature on the precursor decomposition: a reduction of Fe^{3+} in Fe^{2+} simultaneously with the departure of two stearate chains which decompose into ketone, water and CO_2 (which is observed thermally in the nucleation temperature range (200-300°C)). Indeed, a decarboxylation catalyzed by iron(III) cations, leading to a reduction of iron(+III) to iron(+II) has already been reported[18]. Therefore, LCTEM, performed on preheated reaction mixtures, provided usefull informations on the nucleation mechanism.

In addition, most liquid cell TEM experiments have been conducted in water and there are only very few experiments in organic solvents[39–41]. However, even in organic media, these experiments reported always on the presence of small amount of water inducing the presence of radicals to explain the observed reactions. In our case, we use a reaction media, preheated at a temperature lower that those reported for the nucleation step, but which has already began to react/evolve. Thus, such study, quite without water due to the preheating step at 120°C, will shed light on the potential of such technique for mechanistic investigations in organic solvents.

The different stages occurring up to the nucleation step have been analysed by combining these different characterization techniques. We evidenced thus, for the first time, that the nucleation, either in the powder state or in the liquid reaction media, occurs inside nanoreactors with vesicle/droplet aspect in which the reactants are confined.

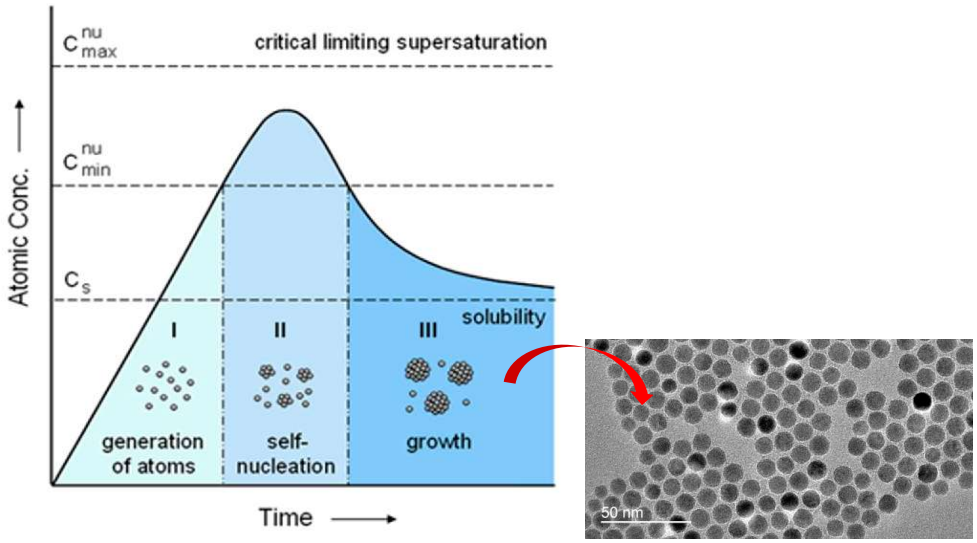

Figure 1. Variation of monomer concentration during nucleation-growth processes (Right: TEM image of 10 nm sized NPs). Adapted from Xia et al[11]

RESULTS

During the 10 nm NPs standard synthesis, the mixture is stirred and heated at 120 °C for 1 h without reflux condenser in order to dissolve the reactants and remove the volatile molecule residues; afterwards, the reaction mixture is heated up to about 290°C at 5°C/min and maintained for 2 hours at this temperature. IONPs with a mean diameter of 10 nm are thus reproducibly obtained (Figure S1). From earlier published results[2,4,14,16] confirmed by investigations on these iron stearates[12], the nucleation of iron oxide NPs occurs in the range 200-300°C with the observation of stable nuclei from around 280°C. In this whole temperature range 200-300°C (Figure S5)[12], a high weight loss is also noticed related to the vanishing of carboxylate chains[13] and more precisely to the loss of two stearates for $FeSt_2$, whose composition is $[Fe_3(\mu_3\text{-}O)St_6.xH_2O]Cl$[17]. We have thus investigated the thermal behavior of iron stearate powders before and after 200°C and performed LCTEM on the reaction mixture after the preheating treatment at 120°C.

Thermal transformation steps of the iron stearate powders up to 200°C

DSC and SWAXS experiments on iron stearate powders before the beginning of the nucleation step (below 200°C).

SWAXS and DSC analyses provided complementary information on the structural evolution of the iron stearate precursors with temperature (Figures S6-S7). These analyses are described in SI part. $FeSt_2$, with the main composition $[Fe_3(\mu_3\text{-}O)St_6.xH_2O]Cl$, displays a lamellar rotator (Lam) structure consisting of alternating ionic layers and double-layers of alkyl chains crystallized in a two-dimensional hexagonal rotator lattice (Figure 2) [42,43]. $FeSt_{2d}$ is on the contrary an amorphous solid composed of a mixture of $[Fe_3(\mu_3\text{-}O)St_6.xH_2O]St$ and of polynuclear complexes (polycations) with higher Fe content (formula $[Fe_7(\mu_3\text{-}O(H))_6(\mu_2\text{-}O(H))_xSt_{12-x}]St$) in agreement with the characterizations described in SI. In fact, several species are certainly formed during the prolonged annealing of $FeSt_2$ at 140°C leading to $FeSt_{2d}$ and the associated 12% weight loss reduced the stoichiometry in stearate in an inhomogeneous way. The presence of polynuclear complexes with higher Fe content and lower Fe/St ratio is in agreement with such observation of stearate chain elimination. Nevertheless, a brief fluidification at 120°C led to its reorganization into a hexagonal columnar liquid crystal (LC) and a Lam structure was recovered on subsequent cooling (Figure S6). A hexagonal columnar LC was also formed for $FeSt_2$ above its melting temperature lying around 100°C. Expectedly, both compounds showed different transition temperatures to isotropic liquid (140°C for $FeSt_2$ and 175°C for $FeSt_{2d}$), since their stoichiometries are different (Figure S8). All these DSC and SWAXS experiments show that after a heat-treatment to 120°C of both stearates and a cooling down to room temperature, the lamellar structure is recovered. They confirm also that crystalline phases entirely vanished after the heat-treatment step at 120°C to homogenize the reaction mixture during the NPs synthesis process.

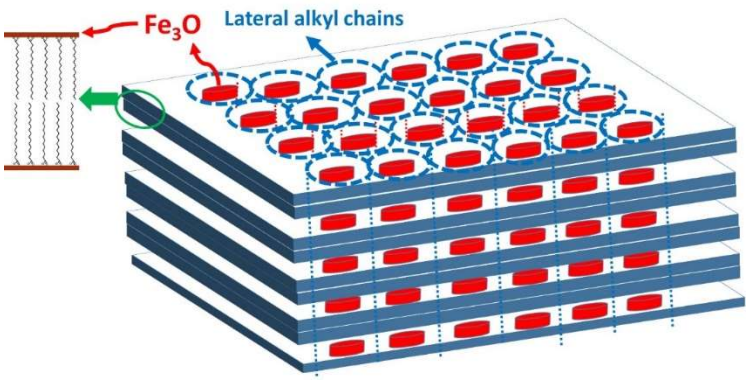

Figure 2. Schematic structure of $FeSt_2$: planes with hexagonal arrangement of polynuclear iron complexes separated by double layers of all-trans stearate chains perpendicular to polynuclear complex planes.

TEM experiments under vacuum below 200°C

TEM experiments at different temperatures were performed on $FeSt_2$ powder deposited on an amorphous carbon film of a TEM grid (Figure 3). The flakes of the lamellar compound are visible in the TEM image taken at room temperature. Heating the powder in a TEM heating stage leads to the morphological transformations shown in Figure 3. Slightly above 100°C, the compounds start melting and form droplets-like structures. A coalescence of these droplets is also observed and explains the observation of different droplet sizes. Below 200°C, the SAED patterns (Figure 3) show that these droplet-like particles are amorphous in agreement with previous DSC and SWAXS experiments. After cooling, amorphous solid objects with a globular morphology remain.

To get information about the speed of such transformations, short heat pulses can be applied instead of continuously heating of the specimens. This has been done by sending infrared nanosecond laser pulses onto the compounds in the TEM and observing their transformation. Under laser pulses of moderate intensity (1064 nm, 7 ns), the same morphological transformation of the powder as under continuous heating is observed (figure S9). After one pulse (25 µJ on a specimen area of 150 µm in diameter), the effect of melting and coalescence is already obvious. Since the specimen is heated within 7 ns (duration of the IR pulse) and cools down within some tens of microseconds, the structural transformations are very fast. The delay between the IR pulses was several seconds to minutes so that the specimen was always at room temperature when the images were taken. Repeated IR pulses lead to ongoing coalescence of the vesicles.

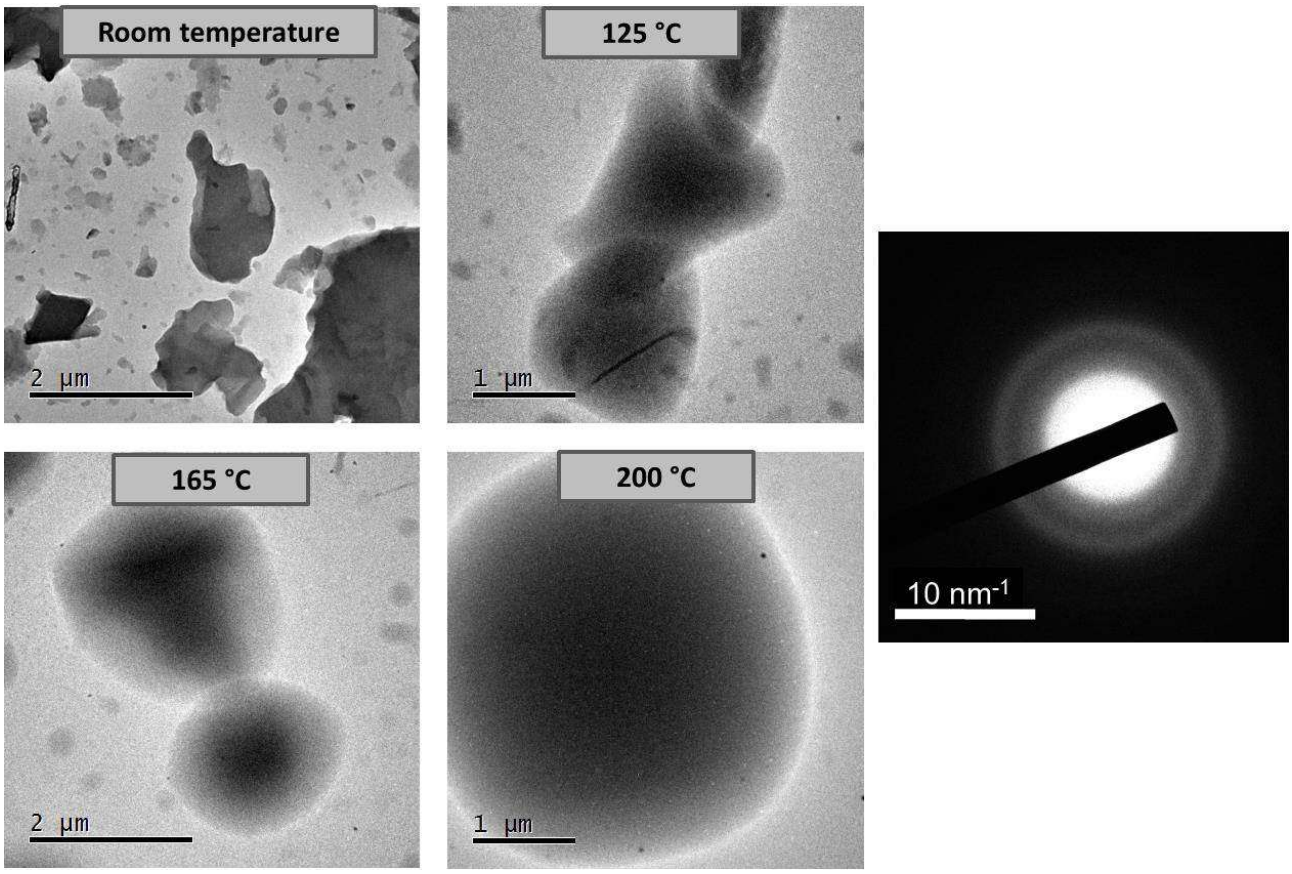

Figure 3. TEM images taken from powders of $FeSt_2$ (left) as a function of temperature and SAED pattern at 200°C (right).

Thus, continuous heating of $FeSt_2$ particles (Figure 3 and Figure S9) leads first to the melting and transformation of the flake-like structure of iron stearate particles into spherical droplet-like particles. Up to 200°C, the particles remain amorphous and tend to coalesce.

TEM experiments under vacuum in the temperature range 200-280°C

Figure 4 and Figure S10 show the evolution of the iron stearate particles under static heating in vacuum at temperatures above 200°C. Above 220°C, the droplet-like particles appear to be surrounded by another phase (shell with lower contrast, Figure 4b-c and Figure S10). This shell of 200 – 300 nm thickness shows less electron scattering, due either to the absence of heavier elements such as Fe (which should prevail in the darker core) or due to the absence of a crystalline phase that diffracts the beam (the images were taken under multi-beam conditions). This shows that a separation into two phases occurred above 200°C. The weak contrast of the shell despite its considerable thickness indicates an organic (hydrocarbon) material that doesn't contain considerable amounts of iron.

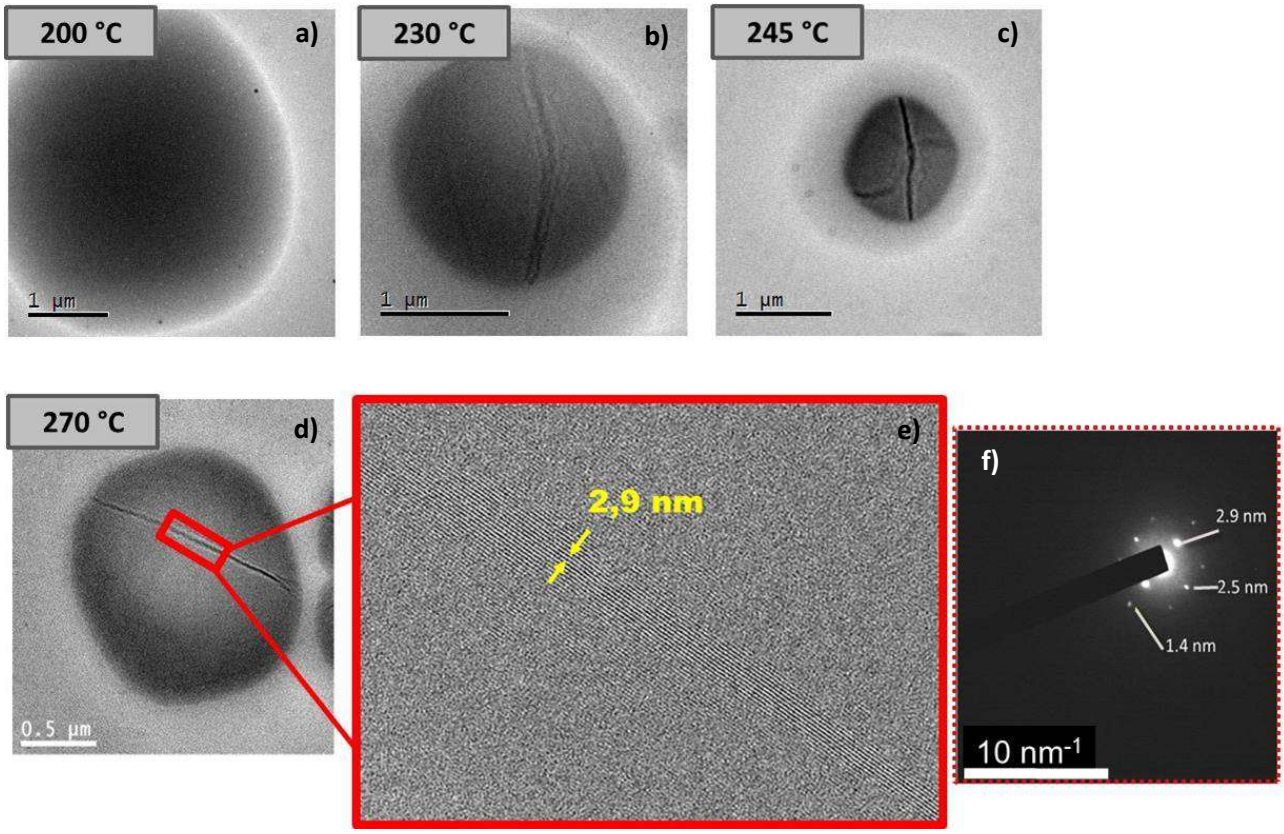

Figure 4. TEM images of $FeSt_2$ powders in the temperature range 200-280°C (a-d). In the low-magnification images (b-d), the dark lines correspond to planar defects in a crystalline structure. At high resolution, the lattice of the crystalline Fe_2St phase is getting visible. (e) shows a HRTEM image including the defect in (d). The diffraction pattern (f) shows the corresponding reflections. The amorphous shell around the droplets is visible in (b) and (c).

Above 200°C, a crystallization of the droplet-like particles is observed (Figure 4) and occurred quite simultaneously with the appearance of the white shell around the droplets. The crystalline phase remains stable upon further heating up to 270°C. Above 220°C, the particles seem fully crystallized without a visible loss of volume with respect to the droplet-like particles below 175°C. In many particles, diffraction contours along a crystal defect are visible as dark lines (Figure 4 c-e and Figure S11). These defects could be grain boundaries separating different crystal orientations or cracks resulting from thermal chock (Figure 4e). Subsequent cooling of the system showed that these transformations are irreversible and the crystalline structure persists upon cooling to room temperature. The largest interplanar spacings are 2.9 and 3.2 nm. They appear to be characteristic for a molecular crystal and they are much larger than typical lattice spacings of oxides. On the other hand, the observed spacings are lower than the interlamellar distances measured in $FeSt_2$ (*d(001)* = 4,95 nm ≈ 2L (L= length of a stearate chain) and indicate a partial interdigitation of stearate chains or the presence of an angle between the iron layer and the alkyl chains as described in Figure S12. Indeed, upon heating, there is a melting of stearate chains (cf. SI part and Figure S6), which affects the interlamellar distances and their local organization. In addition, we know that there is also a loss of two stearate chains in the range 200-300°C and the crystallization occurs quite simultaneously with the formation

of the white shell around droplets. We suggest thus that the observed crystallisation occurs simultaneously with the loss of stearate chains. Such a loss would induce a re-organisation of iron stearates leading to a crystalline phase. One may notice that in this temperature range, the beginning of a condensation between Fe_3O units in Fe_3OSt_6 complexes has been reported previously [2,44,45],[46].

TEM experiments in vacuum above 280°C

Above 280°C, the transformation of the molecular crystal to iron oxide nuclei is observed (Figure 5 and Figure S13). The average sizes of the oxide crystals are approximately 5-10 nm at 300°C. The diffraction pattern allows identifying the FeO (wüstite) phase (Figure 5). This is in agreemen with previously published results which have already demonstrated that the nuclei appear in the wüstite phase[13].

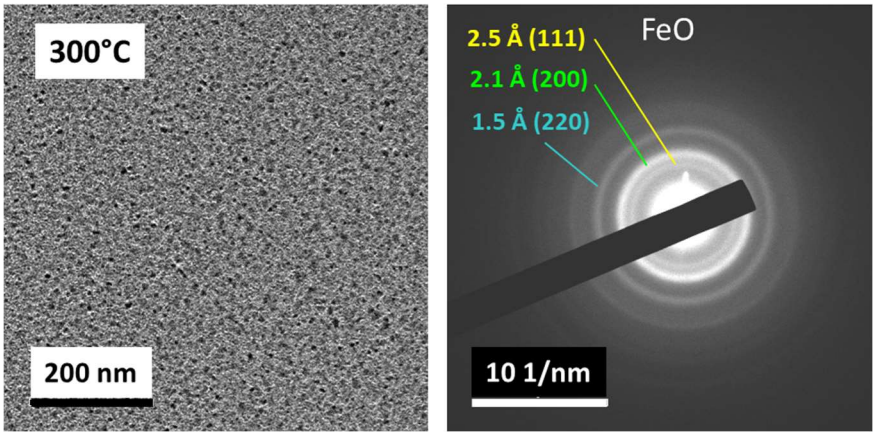

Figure 5. Characteristic TEM image at 300°C showing the nucleation of iron oxide nanocrystals (left). The diffraction pattern (right) shows the diffraction rings of FeO.

Fast heating with nanosecond IR pulses. Besides static heating, the *direct* transformation of iron stearates to oxide NPs is also possible by heating with short IR laser pulses. Several IR pulses with moderate intensity (to avoid evaporation) were applied. A complete transformation from stearate flakes to oxide crystals needs several pulses (in spans of several seconds between the pulses) but the crystalline intermediate phase did not appear. These experiments, which are described in the SI part (§ fast heating by using laser pulse, Figures S14-S17), allow concluding that the transformation of iron stearates to oxide nanocrystallites occurs at the microsecond timescale if the temperature during the laser pulses is high enough. Since the formation of the crystalline molecular phase does not occur under laser pulses, we can conclude that the crystallization of the stearate phase is slow and only appears under close-to-equilibrium conditions. Furthermore, this phase doesn't seem to be a necessary step in the nucleation of oxides

These high-temperature TEM results are in agreement with earlier results, which reported the nucleation of oxide crystals around 280°C. They strongly suggest that the nucleation occurs in confined systems (droplet like nanostructures which can be assimilated as nanoreactors), which originate from melting of stearate particles.

Study of liquid reaction media in organic solvent pre-treated at 120°C.

After these investigations on powders, further characterizations have been performed on reaction media solutions, consisting of a liquid mixture of iron stearate, oleic acid in dioctylether solvent, which has been submitted to a homogeneisation treatment at 120°C for 60 min. Such reaction mixture leads during the TD process up to 290°C to IONPs with a mean size of 10nm (Figure S1).

SWAXS Characterisation. After such a "solubilisation" step of reactants at 120°C, the resulting cooled mixture solutions were analyzed by SWAXS (Figures 6a and S18). SWAXS patterns show that they form suspensions of the same lamellar rotator phase as powder systems (Figures S6 and 6a). Such liquid mixtures pass the Krafft temperature around 40°C. At 60°C, a clear solution is obtained and all reflections vanish, leaving only the broad scattering signal at 1.4 $Å^{-1}$ from solvent molecules interactions. Nevertheless, a scattering upturn is clearly visible at small angles, which indicates presence of aggregates in solution. To specify the aggregation nature, two diluted solutions of $FeSt_2$ (volume fractions Φ_V = 0.0087 and 0.0171) in dioctylether and in presence of 2 equivalents of oleic acid were recorded in SAXS at low angles, subtracted from solvent and renormalized (Figure 6b). The low-angle scattering signal clearly confirms that aggregates subsist in solution at 100°C, thus far from the Krafft temperature. However, the scattering profiles are different for both concentrations, revealing that there are no aggregates of defined size and isolated in solution. At the highest concentration, the steeper decrease of the scattering should indicate a larger average aggregate size. A quantitative analysis is not possible given the profile shape variation between concentrations.

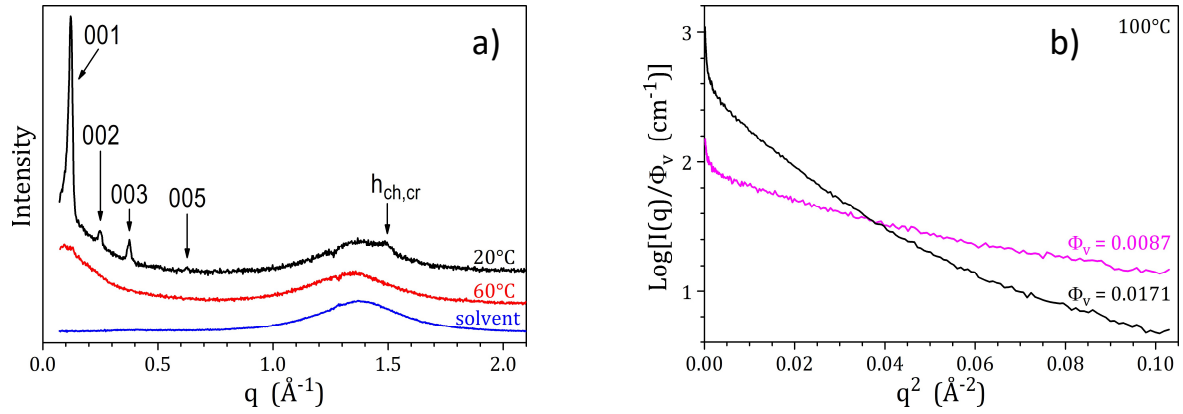

Figure 6. a) SWAXS patterns of standard 10 nm NPs reaction mixture at 20°C and 60°C using $FeSt_2$ ($FeSt_{2d}$ in Figure S18), as compared to solvent (dioctylether). b) Guinier representation of SAXS data for two volume fractions of $FeSt_2$ in dioctylether and in presence of 2 equivalents of oleic acid. Scattering curves were recorded at 100°C, subtracted from solvent and renormalized.

DLS measurements. The presence of "nanostructures" in the reaction media upon heating up of the system was further confirmed with DLS measurements as a function of temperature (Figure S19)**.** At low

temperatures, “structures” with hydrodynamic diameter in micrometer size range are observed in particle size distribution measurements. When the temperature becomes higher than the melting temperature of $Fest_2$ (60°C), a clear decrease of the mean hydrodynamic size is noticed (Figure S19). Therefore, these DLS measurements suggest strongly the presence of nanostructures in the heated reaction media which size decreases when the temperature increases.

Liquid AFM technique. Preheated reaction media was deposited just after the heating step on a functionalized substrate for observation with an original liquid AFM technique in an organic solvent. Liquid AFM images are given in Figures 7a and S20 and revealed a homogeneous distribution of nanostructures over the whole surfaces just after deposition on the substrates. From the AFM images, at least two populations with different sizes can be measured. Interestingly, the size distributions are quite monomodal. $FeSt_2$ presents a major population around 53±6 nm and a second one around 74±7 nm when the heat-treated precursor $FeSt_{2d}$ presents two populations equivalent in presence at around 37±6 and 17.5±4 nm.
Those nanostructures are observed to spontaneoulsy assemble to form “rings” as seen for $FeSt_2$ in Figure 7a. Indeed, we observed an ageing effect. If AFM is not performed just after the heating step but after cooling down the reaction mixture and some ageing time, a coalescence of the nanostructures is observed leading to nanostructures with submicronic-micronic sizes (Figure 7 b-c). This would explained DLS measurements with a decrease of the nanostructure size when the temperature increases as well as SWAXS experiments at different concentrations. In liquid, the size of these nanostructures would decrease with the temperature increases and when the temperature decreases, they coalesce into bigger nanostructures.
AFM profiles on these submicronic nanostructures (Figure 7d and Figure S21) suggest that they consist in stacked layers/sheets. The measured lamellar distance is in agreement with that of the pristine iron stearate (*d(001)* = 49.5 Å ≈ 2L (L= length of a stearate chain)) confirming again that, under cooling, the lamellar structure is recovered.

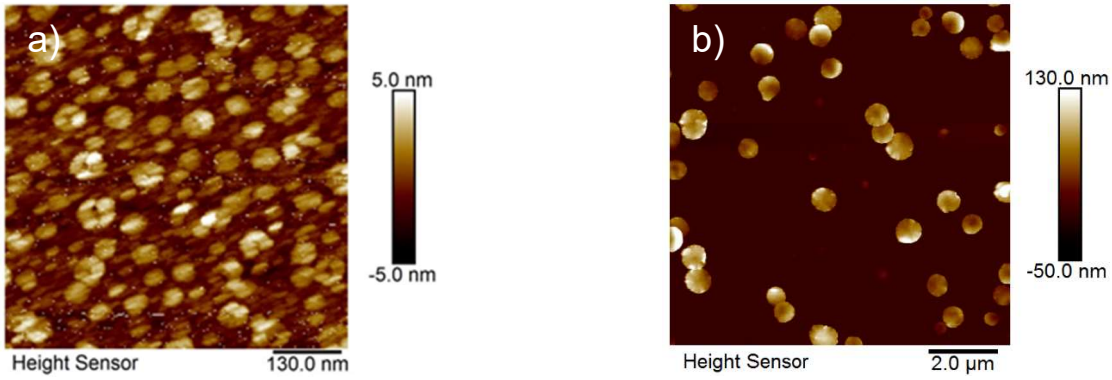

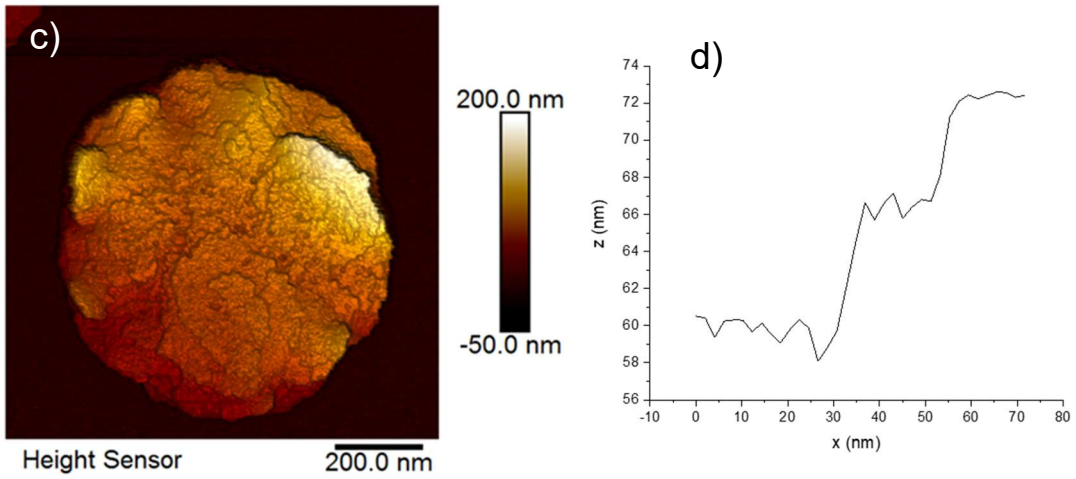

Figure 7. liquid AFM just after deposition on a functionalized substrate of the "just prepared" pre-heated mixture (reaction mixture with $FeSt_2$) a) and after ageing b). High magnification of "aged" nanostructures c) and AFM profile of an "aged" nanostructure d) from figure c).

CryoTEM. Cryo-TEM allowed investigating a thin vitrified film of the reaction media solution in which all processes are stopped by plunge-freezing in an appropriate coolant[26]. The organisation/structuration of nanostructures in assemblies of nanosheets or stacked sheets has also been evidenced by cryoTEM performed on $FeSt_{2d}$ reaction mixture (Figure 8). The presence of iron in these nanostructures has been confirmed by EDS analysis and also by classical EDX elemental mapping during TEM analysis in vacuum detailed in SI part (Figure S22).

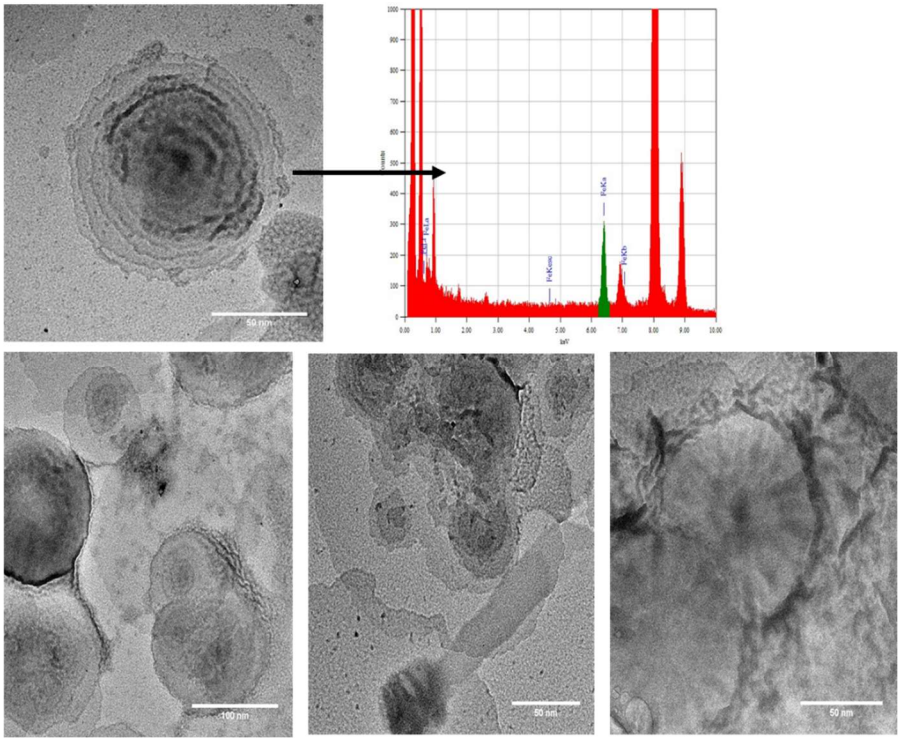

Figure 8. CryoTEM images after freezing of reaction media with $FeSt_{2d}$ and EDS spectra showing the presence of iron (green peak) in these nanostructures.

LCTEM study of reaction mixture preheated at 120°C in organic solvent. A reaction mixture involving all the reactants for the synthesis of the standard 10 nm spheres with $FeSt_{2,d}$ was imaged by TEM in the liquid cell in organic media just after the homogenisation step at 120°C for 60 min. The *in situ* cell TEM image is given in Figure 9 and evidences the presence of spherical structures. Indeed, after a given time of irradiation with the electron beam, $FeSt_{2d}$ reaction mixtures present two populations of spherical structures (Figure 9). The first population presented a sharp dark/grey contrast homogeneous within the structure with a mean size centred on 15 nm. The second population is characterized by a lighter intensity. The size of this last structure is in the range 30-50 nm and their characteristics are typical of droplets. Note that the dioctylether solvent was imaged alone and no bubbles/dropplets were observed in this case under the same irradiation conditions. Considering the atom mass and the composition of the reaction mixture, the dark/grey droplet-shaped nanostructures are expected to contain iron. This additional analysis confirms the hypothesis that such nanostructures originate from the reaction mixture. The observation of such nanosized structures is an agreement with the previous results demonstrating the presence of nanostructures in preheated reaction media.

LCTEM images (Figure 9) as a function of the irradiation time of the reaction mixture showed further that both white and grey nanostructures are preserved and that the nucleation occurs only in dark nanostructures. Indeed, dark points appear in the grey nanostructures when the irradiation time increases and are in particular visible in Figure 9H. These observations similar to those during TEM experiments in temperature support that the nucleation occurs in confined media. Iron oxide NPs have been observed at the end of both experiments conducted with only the iron stearate powder (Figure 5) or the reaction media (Figure S23). The iron oxide nuclei obtained during TEM experiments have a wüstite composition, which is in agreement with previous results[13], when their composition is that of the spinel iron oxide during LCTEM experiments (Figure S23). The measured lattice spacing values given in the Figure S23: (220) (0.287 nm) and (022) 0.242 nm are very close to those of the iron oxide spinel structure. Indeed, the nuclei were in contact with air during these spacing neasurements and it is well known that Fe^{2+} are very sensitive to oxidation at the nanoscale[13,47].

Concerning the white nanostructures, there are several hypothesis: one hypothesis could be that they consist in vesicles stabilized by a double layer of oleic acid. Indeed the amount of oleic acid added is very high and should favor the reversed vesicle formation[48–50]. However, their “inner” intensity is very different from that of outside liquid and thus they can not be assigned to such reverse vesicles. Such “white” bubbles have also been observed during LCTEM in presence of water and attributed to radiolysis of water leading to H_2 bubbles[51]. However in our case, we are in organic solvent and the mixture has been preheated to 120°C and thus the presence of water should be scarced. Considering the high amount of white bubbles and the reaction conditions, such white nanostructures should not be due to radiolysis of water. In fact, the observations that

i) the formation of iron oxide nuclei is observed under electrom beam irradiation and ii) that the nucleation mechanism is induced by condensation of iron stearate radicals resulting from a reduction of Fe^{3+} in Fe^{2+} in iron stearate polycations simultaneously with the departure of two stearate chains which decompose into ketone, water and CO_2, led us to make the hypothesis that the white bubbles could consist in CO_2 bubles. However, water is also generated by the decomposition of stearate chains and thus radiolysis of water is not to exclude. In addition, even if very few LCTEM studies have delt with organic solvents, it has also been reported that a gaseous radiolysis product of ethanol would be H_2 [39,41] and the radiolysis of ethers [52] leads to H_2 formation. Hydrocarbons have been reported as radiolytic products of fatty acids[53]. Therefore, H_2 bubbles are not completely to exclude.

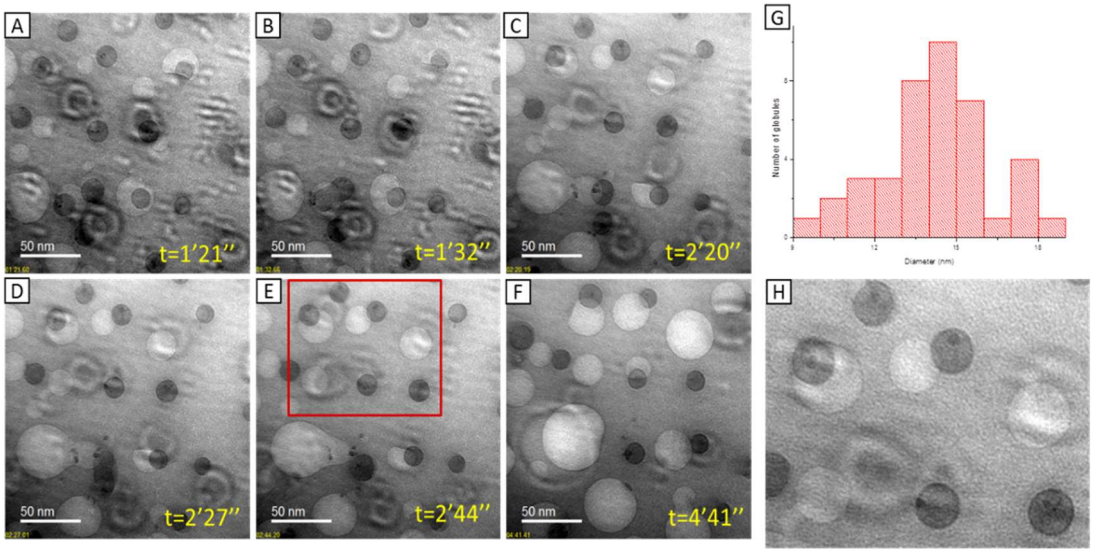

Figure 9. In situ liquid cell TEM experiments of some representative areas from reaction medium with $FeSt_{2d}$ after different exposure times to the electron beam (A-F) and histogram of the size distribution of the contrasted structures (G) and the zoom of the red rectangle area from (E) in (H).

By analyzing the recorded videos as a function of irradiation time (cf. one characteristic video in SI), we noticed that in some dark nanostructures, some black nuclei formed but then redissolved (cf. enclosed video and inside yellow circles in Figure 10). By contrast, when nuclei seem to be enough stable, they are ejected outside the black nanostructures (inside red circles in Figure 10). This phenomenon is observed several times in video. Some nanostructures are observed to merge (Figure 10, green circles) and then some nuclei are formed and ejected. Such observations confirm the LaMer mechanism but evidence also that the nucleation occurs in confined droplet-like nanostructures acting as nanoreactors. Such mechanism explains why there is a very efficient and clear separation of nucleation and growth steps.

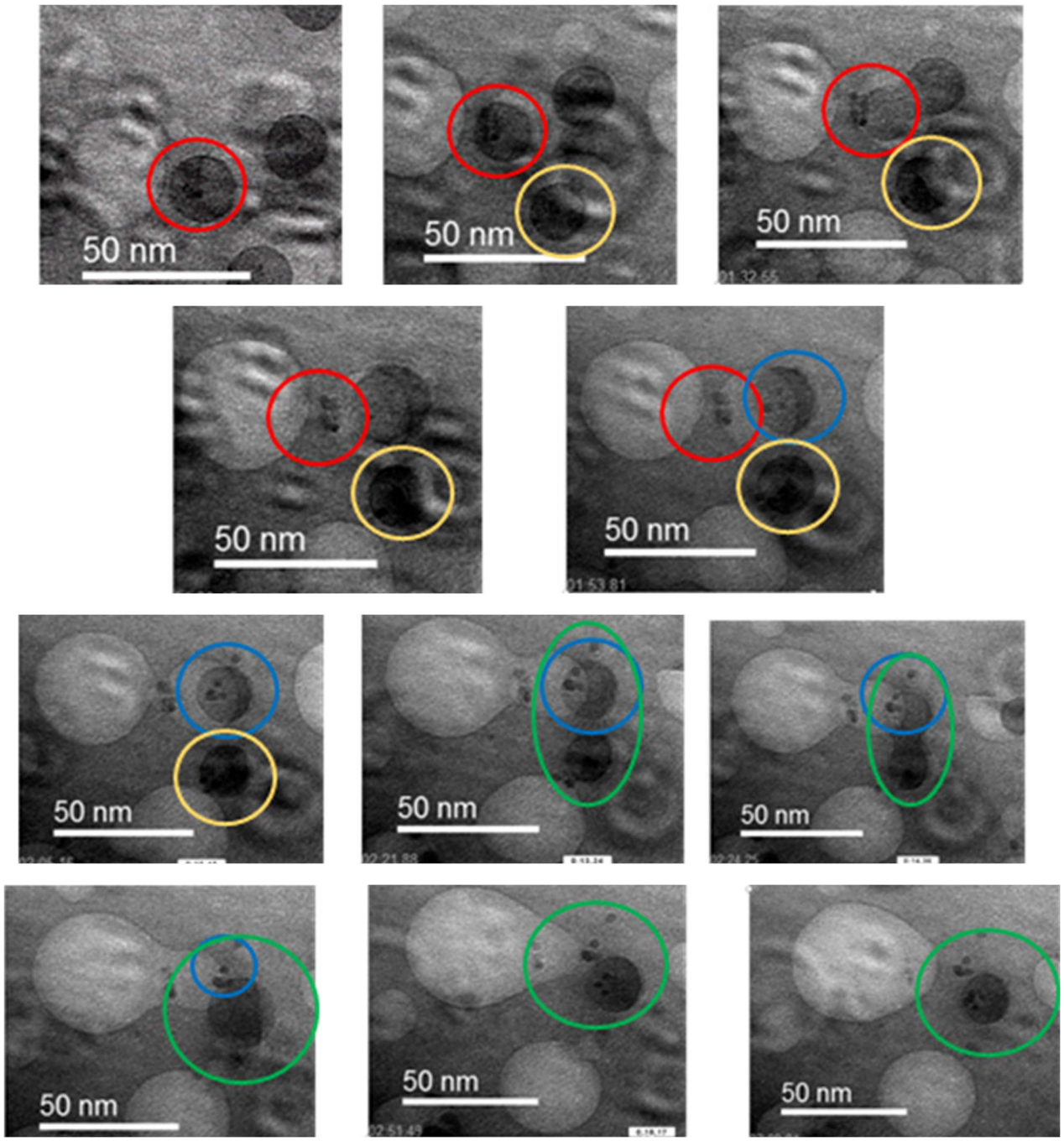

Figure 10. In situ liquid cell TEM images as a function of irradiation time. Red circles: formation of nuclei inside droplet-like nanostructures and then ejection of nuclei from these nanostructures; yellow and blue circles: nuclei formed inside nanostructures which "redisolve"; blue circles: merging/coalescence of two nanostructures leadding to nucleation and further nuclei ejection.

DISCUSSION

The general physico-chemical steps observed from the iron stearate precursors ($FeSt_2$, $FeSt_{2d}$), either in the powdered state (Figure 11) or in the reaction mixture (Figure 12), to the IONPs formation have been summarized in the simplified cartoons presented in figures 11 and 12.

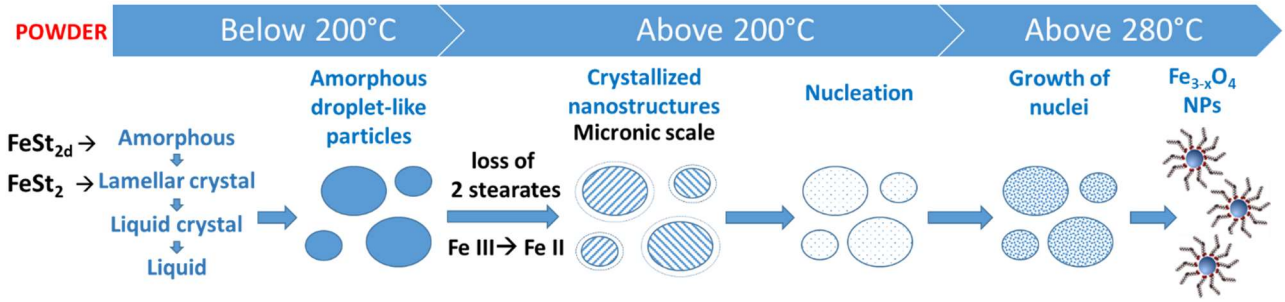

Figure 11. Scheme of the events with the iron stearate powders heated from room temperature up to IONPs formation. The steps above 200°C have been obtained from high temperature TEM experiments.

DSC and SWAXS experiments on powders demonstrated that, after heating up to 120°C (the homogenization temperature of the reaction mixture) and cooling down, both stearates recovered the lamellar structure and that when heating above 140°C ($FeSt_2$) or 175°C ($FeSt_{2d}$), an isotropic medium is obtained. TEM on powders at high temperature showed that iron stearate particles melt and form droplet-like particles (Figure 11), which can merge when the temperature increases and are amorphous below 200°C (in agreement with DSC and SWAXS experiments). The characterizations done on the reaction mixture (heat-treated at 120°C) by SAXS, liquid cell TEM and AFM evidenced the presence of very small droplet-shaped nanostructures with two size distributions (Figure 12). Liquid AFM and cryoTEM demonstrated that nanostructures obtained from a reaction mixture heat-treated at 120°C and cooled down consist of stacked planes/sheets in agreement with SWAXS experiments, which show that the lamellar structure is recovered on cooling down. LCTEM images showed that the smallest nanostructures are dark and contain iron when the biggest ones are white and could be tentatively assigned to CO_2 and/or H_2 bubbles (Figure 12).

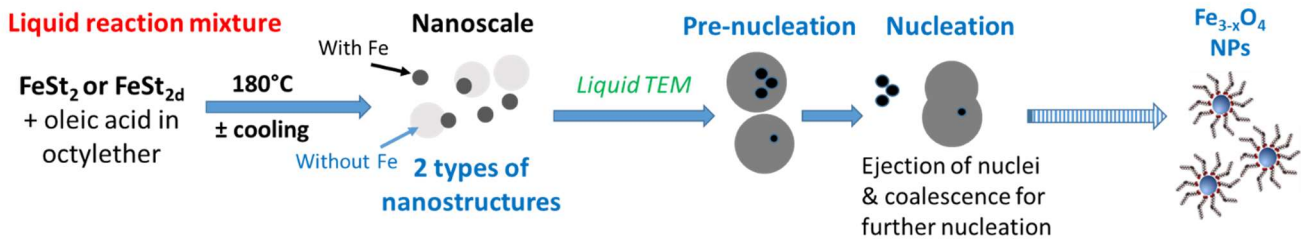

Figure 12. Characterization of the liquid reaction mixture after the homogeneization step at 120°C by different techniques: 1) evidences of the presence of two types of droplet-like nanostructures: **$FeSt_2$:** *AFM:* 53±6 & 74±7 nm and *TEM* observations. **$FeSt_{2d}$**: *AFM:* 17.5±4 & 37±6 nm, *Liquid cell TEM*: 30-50 nm & 15 nm, *DLS in T:* when T>60°C, size distribution decreases, (white droplet-like nanostructures correspond to gas buble when dark droplet-like nanostructures consist of iron stearates) and 2) schematic evolution of the liquid reaction mixtures in LCTEM leading to iron oxide NPs.

The difference in size of nanostructures between those observed by TEM at high temperature on powders and those observed by Liquid TEM&AFM and in temperature DLS measurements on reaction

mixture suggested that both dioctylether solvent and oleic acid in the reaction mixture should contribute to stabilize smaller nanostructures when the temperature increases. Oleic acid is an amphiphilic molecule suitable to generate “reverse “vesicles in organic solvent. The melting of lamellar iron stearate compound in the reaction mixture should be associated with their stabilization by oleic acid in dioctylether. Oleic acid would interact around melted iron stearates and should also contribute to decrease the size of droplet-like nanostructures. The formation of such metallic based reverse vesicles in organic solvent has been poorly reported[54].

At higher temperature than 200°C, TEM on $FeSt_2$ powder shows that droplet-like particles are always present and mainly amorphous but a molecular crystallization is observed above 200°C at the beginning of the nucleation (200-280°C). Nuclei appear clearly in the globular particles from 280°C at the already reported nucleation temperature. Lassenberger[16] observed also by SAXS a diffracting structure before the nucleation takes place. We may notice that the observed molecular crystallisation occurs simultaneously with the appearance of a white halo (purely organic, no Fe atoms are present), which surrounds the droplet-like particles above 200°C. We know that during the nucleation step, there is departure of 2 stearate chains and simultaneously Fe(III) cations are reduced in Fe(II). Both phenomena occur in the temperature range 200-300°C. Therefore, one may attribute the white halo to the released stearate chains around nanostructures (Figure 11). The molecular crystallisation is really observed from 230-250°C and interplanar distances corresponding to interlamellar distances different from those observed in native iron stearates (suggesting a partial interdigitation of stearate chains) are noticed. Further works are still needed to identify the crystalline molecular phase, which is formed before the nucleation.

Nuclei are observed within nanostructure when powders were heated at higher temperatures. In reaction mixture, LCTEM allowed evidencing that the nucleation occurs in dark/iron rich vesicles. As soon as the nuclei are formed, they are then are ejected outside the nanostructures/nanoreactors (Figure 11 and video) but the nanostructure remains stable.

We have also performed a standard IONPs synthesis experiment up to 280°C and then observed the reaction mixture by TEM. As shown in Figure S24, such droplet-like nanostructures were identified confirming that this confined nucleation occurs also in standard conditions.

As metals are well-known to form self-assembled lamellar structures in the presence of long chain carboxylic acids, this mechanism involving confined nanoreactors should be relatively general for most metal oxides NPs obtained via thermal decomposition in organic solvent in the presence of complexing surfactants such as long chain organic acids. Indeed, we have also observed the formation of such nanostructures during the synthesis of manganese oxide nanoparticles (Figure S25). In addition, such a new confined nucleation mechanism in organic solvent in nanoreactors composed of long carboxylate chains coordinated to iron polynuclear complexes would explain the high difficulties in obtaining IONPs doped homogneously by other metal cation[55–58]. Indeed, the doping elements should need to be integrated in the nanoreactors. Such

nanostructures would also explain why IONPs formed easily at the surface of carbon materials such as carbon nanotube or few layer graphen[59–61]: the alkyl chains at the periphery of the nanoreactors should favor their anchoring at the surface of carbon materials.

CONCLUSION

We have investigated the thermal behavior of two iron stearates used as iron precursors in the TD process by using different techniques such as SWAXS, SAXS, liquid AFM, liquid cell TEM, and in situ TEM at high temperature. All experiments performed on powders and preheated reaction media evidenced for the first time the formation of droplet-like particles resulting from the melting of iron stearate particles during the temperature increase. The reaction mixture containing long chain carboxylic acid (oleic acid) and dioctylether led to smaller droplet-like nanostructures due to temperature and surfactant stabilization effects. Then, when the iron stearates begin to lost stearate chains in the nucleation temperature range, a molecular crystallisation of these nanostructures is observed. Further studies will aim at characterizing this crystalline phase. Finally, the nucleation occurs within these droplet-like nanostructures, acting as nanoreactors and when nuclei are formed and stable, they are ejected from these nanostructures suggesting that the growth occurs outside these nanostructures. This nucleation confined in nanostructures in organic media explains why the nucleation and growth steps are well separated in the TD process. The observed behaviour can be described as a Lamer process driven via precursors confinement. Such mechanism of confined nucleation is demonstrated for the first time thanks to a combination of fine *in situ* characterization techniques and paves the way towards a better mastering of structural NPs parameters. As most metals form self-assembled lamellar structures in the presence of long chain organic acids, this nucleation mechanism in confined nanoreactors should be relatively general for many NPs of divalent and trivalent metal oxides obtained via thermal decomposition in organic solvent in the presence of complexing surfactants such as long chain organic acids.

MATERIALS AND METHODS

Synthesis of both iron stearate precursors. Iron stearate (II) named $FeSt_2$ was prepared following a previously reported protocol **[12]** (detailed in SI) by precipitation of sodium stearate and ferrous chloride salt in an aqueous solution. $FeSt_2$ is a lamellar compound with the composition $[Fe_3(\mu_3\text{-}O)St_6.xH_2O]Cl$ and mainly Fe III cations.

Heat treatment on $FeSt_2$ was performed in an oven at 140 °C for 48h and the resulting compound was named $FeSt_{2d}$. Its structure and composition are detailed in SI part. $FeSt_{2d}$ is amorphous and display two main

polynuclear complexes (polycations) (Figure S4): $[Fe_3(\mu_3\text{-}O)St_6.xH_2O]St$ and another one with higher Fe content (formula $[Fe_7(\mu_3\text{-}O(H))_6(\mu_2\text{-}O(H))_xSt_{12-x}]St$).[12,13] and with only Fe III cations[44].

Synthesis conditions of iron oxide NPs with a mean size of 10 nm. IONPs are synthesized from an already reported reproducible protocol[10] which consist in the TD of the synthesized iron stearate in presence of oleic acid (OA, 99%, Alfa Aesar) in dioctylether (OE, 99%, Sigma). The as synthesized iron stearate (1.38 g for $FeSt_2$ and $FeSt_{2d}$, 2.2 mmol in iron) is mixed with OA (1.24 g, 4.4 mmol) in 20 ml of OE in a two neck RBF. The mixture is stirred and heated at 120 °C for 1 h without reflux condenser in order to dissolve the reactants and remove the volatile molecules residues. We demonstrated earlier that if the heating step at 120°C is suppressed, the mean size is smaller[22]. The hypothesis was that such volatiles molecules residues and in particular water would affect the thermal stability of the iron complex.

Preparation of "reaction mixture". Characterizations have been conducted on samples consisting of "reaction mixtures" after this mixing step at 120°C (and a cooling down or just/directly after the treatment at 120°C).

Synthesis of iron oxide nanoparticles. After the previous mixing step at 120°C, the cooler is then connected to the flask and the solution is heated to the boiling temperature (≈ 290 °C) with heating rate of 5 °C/min and heated to reflux for 2h under air. After cooling to RT, a black suspension is obtained which is solubilized in 10 ml of chloroform. The NPs are then precipitated by the addition of an excess of acetone the first time and washed three times with chloroform and acetone at a ratio of 1:4 at 14000 rpm for 5 min by centrifugation. The NPs can finally be suspended in 50 ml of THF.

The NPs synthesized using either $FeSt_2$ or $FeSt_{2d}$ display a mean diameter of 10.3 ± 0.8 and 10.2 ± 0.9 respectively (Figure S1a-b). We have also synthesized IONPs by decomposing only $FeSt_2$ (without solvent and oleic acid) and slightly oxidized magnetite NPs, with a mean size of 11.9 ± 2.3 nm and a rather spherical shape, were obtained (Figure S1c).

Characterization techniques

Differential scanning calorimetry (DSC) measurements were performed with a TA Instruments DSCQ1000 instrument operated at a scanning rate of 5 °C min^{-1} on heating and on cooling.

SWAXS (Small and Wide Angle X-ray Scattering) measurements were performed with a transmission Guinier-like geometry. A linear focalized monochromatic Cu $K_{\alpha 1}$ beam (λ = 1.5405 Å) was obtained using a sealed-tube generator (600 W) equipped with a bent quartz monochromator. The samples were filled in home-made sealed cells of 1 mm path. The sample temperature was controlled within ±0.01 °C, and exposure times were varied from 2 to 24 h. The patterns were recorded with a curved Inel CPS120 counter gas-filled detector and on image plates scanned by STORM 820 from Molecular Dynamics with 50 µm resolution.

SAXS (Small Angle X-ray Scattering) measurements were performed at the Institut Charles Sadron (ICS), CNRS-UPR 22, France, with Rigaku diffractometer operating with a microfocus rotating anode generator (Micromax-007 HF, 40 kV 30 mA, Cu Kα radiation, λ = 1.54 Å). The X-ray beam was monochromatized and

focused with Confocal Max-Flux Optics (Osmic) fitted with a three-pinhole collimation system. The beamstop was equipped with a PIN diode to determine the transmission factor. In the SAXS configuration, the intensity was collected with a 2D multiwire camera located 0.81 m from the sample and covering a scattering vector range 0.011 $Å^{-1}$ < q < 0.33 $Å^{-1}$ (q is defined as $4\pi/\lambda \sin(\theta/2)$, where θ is the scattering angle). Samples were introduced between thin calibrated mica cells (1 mm apart) and sample temperature was controlled within ±0.05°C. The intensities were corrected according to usual procedures. Data were radially integrated, corrected for electronic background, detector efficiency, empty cell scattering, thicknesses, and transmission factors. Fluorescence contribution from iron content was recorded from $FeCl_3$ solution and removed from sample measurements. Scattering from pure solvent was recorded for subtraction from sample measurements.

In-situ TEM at high specimen temperature. The stearate samples were deposited onto amorphous carbon grids (thickness 30 nm) and observed by imaging and electron energy-loss spectroscopy (EELS) in an electron microscope. In-situ high-temperature treatment was realized either by continuous heating in a high-temperature specimen stage or by pulsed heating with infrared laser pulses. An ultrafast TEM that allows exposing the samples to laser pulses (7 ns, 1064 nm) was used for these experiments. The combination of continuous with pulsed heating allowed us to compare equilibrium with non-equilibrium dynamics and to obtain an upper limit of the timescale for the TD of stearates.

In situ liquid cell TEM. Liquid cell transmission electron microscopy is a method, which allows to study liquid specimens[28]. Inside the TEM, a high vacuum should be generally present and because of this, only solid samples can be analysed in the traditional modes, as the liquid samples are incompatibility with a vacuum environment.[62].

The development of the liquid cell transmission electron microscopy (Figure 13) was possible due to the significant progresses in the fabrication of new windows that are electron transparent, thin enough for allowing reasonable imaging and with a controlled submicrometer separation between the windows where the liquid should be confined. The liquid cell is made of a thin layer of silicon nitride (30-50 nm) which is deposited onto a silicon wafer. The silicon is etched from the back to form a window with dimensions around 100 µm to allow the beam to pass. The wafer is diced into chips that are placed face to face with a spacer material between like in a sandwich[28].

Figure 13. *Left:* schematic representation of the experimental protocol used for the preparation of LC-TEM experiments. First, 2.2 mmol in iron of iron stearate were mixed with 4.4 mmol of oleic acid in 20 mL octylether used as a solvent. The mixture was stirred and heated at 120 °C for 60 min without reflux condenser in order to dissolve the reactants and remove the water residues. 1) one droplet of the previously heated solution was deposited over the bottom chip. 2 and 3) the top chip was placed rapidly over to avoid drying taking care of the proper alignment of the windows. 4) the lid was placed to close the system, fix both chips in position with the screws assuring the proper tightness to avoid any leaking to the TEM column. *Right:* scheme of the LC-TEM set-up and experiments. The thickness between the two SiN membranes is 150 nm.

The liquid cell for the transmission electron microscope is made of two microchips placed together like in a sandwich. All the preparation needs to be done in a place with low dust. A carbon-coated tweezers is used to take the microchips from the storage box and then placed in a beaker with acetone for 2 minutes to remove the coated polymers from the surface of the microchips which protect the membrane. The microchips are transferred from the beaker with acetone and placed 2 minutes in the ethanol and another 2 minutes in the ultrapure ethanol to eliminate completely all the residues. The microchips are removed from the beaker with ethanol and dried using a thin flow of compressed air. All those manipulations are realized carefully to avoid the damage of the cell. The microchips are placed for 5 seconds at Plasma Cleaner to make the surface of the silicon nitride membrane hydrophilic. A light microscope is used to check that membrane doesn't indicate any rupture or fragility.

Atomic Force Microscopy. AFM images were performed under organic solvents (dioctylether, octadecene) using a Bioscope Resolve instrument (Bruker Nano, Palaiseau, France). Silicon wafers were first sonicated in a acetone/ethanol (1:1) bath for 10 minutes and dried under nitrogen flow. After this procedure, silicon wafers were cleaned 30 minutes with UV-Ozone Cleaner (Novascan) and then coated with polydopamine by immersion 15 min in a solution of dopamine at 4g/L in 10 mM TRIS buffer (pH 8). Substrates were extensively rinsed with milli-Q water and then dried under nitrogen flow. 100 µL of NPs suspension were deposited 10 min onto the substrate and then rinsed with the appropriate solvent before imaging. Topographical images were performed by Peakforce TappingTM mode. Silicon nitride cantilevers of conical shape purchased from Bruker (PeakForce Tapping HIRS-FA, Bruker nano, Palaiseau, France) with spring constant of about 0.35 N/m were used for both imaging and mechanical measurements. All images were recorded with a resolution of 256 by 256 pixels and a scan rate of 1 Hz. Sections and Size distribution are obtained with the nanoscope analysis software.

ACKNOWLEDGEMENT. The Region Alsace, France, and the Labex Chimie des Systemes Complexes, University of Strasbourg, France are gratefully acknowledged for the doctoral fellowship to Geoffrey Cotin. This research project was also co-funded by Labex CSC, Alsace contre le cancer, INCA (project PRTK14, THERAMAG 2014-

225), French national agency for research (ANR) under the project InSiChem ANR-16-CE05-0011 and EQUIPEX program of the Agence Nationale de Recherche (France), contract ANR-11-EQPX-0041 (project UTEM). We thank Mr. Guillaume Fleith for realizing the SAXS measurements at the Institut Charles Sadron (ICS), CNRS-UPR 22, France. Pr Clement Sanchez thanks University of Strasbourg Institut of Advanced Study. The authors acknowledge the Spectroscopy and Microscopy Service Facility (SMI) of LCPME (Université de Lorraine-CNRS – http://www.lcpme.cnr-nancy.fr) for AFM analyses.

REFERENCES

[1] J. Park, K. An, Y. Hwang, J.-G. Park, H.-J. Noh, J.-Y. Kim, J.-H. Park, N.-M. Hwang, T. Hyeon, *Nature Materials* **2004**, *3*, 891.

[2] T. Hyeon, S. S. Lee, J. Park, Y. Chung, H. B. Na, *Journal of the American Chemical Society* **2001**, *123*, 12798.

[3] S. Sun, H. Zeng, D. B. Robinson, S. Raoux, P. M. Rice, S. X. Wang, G. Li, *Journal of the American Chemical Society* **2004**, *126*, 273.

[4] S. G. Kwon, Y. Piao, J. Park, S. Angappane, Y. Jo, N.-M. Hwang, J.-G. Park, T. Hyeon, *Journal of the American Chemical Society* **2007**, *129*, 12571.

[5] M. V. Kovalenko, M. I. Bodnarchuk, R. T. Lechner, G. Hesser, F. Schäffler, W. Heiss, *Journal of the American Chemical Society* **2007**, *129*, 6352.

[6] G. Cotin, C. Kiefer, F. Perton, D. Ihiawakrim, C. Blanco-Andujar, S. Moldovan, C. Lefevre, O. Ersen, B. Pichon, D. Mertz, S. Bégin-Colin, *Nanomaterials* **2018**, *8*, 881.

[7] B. P. Pichon, O. Gerber, C. Lefevre, I. Florea, S. Fleutot, W. Baaziz, M. Pauly, M. Ohlmann, C. Ulhaq, O. Ersen, V. Pierron-Bohnes, P. Panissod, M. Drillon, S. Begin-Colin, *Chem. Mater.* **2011**, *23*, 2886.

[8] A. Walter, C. Billotey, A. Garofalo, C. Ulhaq-Bouillet, C. Lefèvre, J. Taleb, S. Laurent, L. Vander Elst, R. N. Muller, L. Lartigue, F. Gazeau, D. Felder-Flesch, S. Begin-Colin, *Chemistry of Materials* **2014**, *26*, 5252.

[9] V. K. LaMer, R. H. Dinegar, *J. Am. Chem. Soc.* **1950**, *72*, 4847.

[10] W. Baaziz, B. P. Pichon, S. Fleutot, Y. Liu, C. Lefevre, J.-M. Greneche, M. Toumi, T. Mhiri, S. Begin-Colin, *J. Phys. Chem. C* **2014**, *118*, 3795.

[11] Y. Xia, Y. Xiong, B. Lim, S. E. Skrabalak, *Angewandte Chemie* (*International ed. in English*) **2009**, *48*, 60.

[12] G. Cotin, C. Kiefer, F. Perton, M. Boero, B. Özdamar, A. Bouzid, G. Ori, C. Massobrio, D. Begin, B. Pichon, D. Mertz, S. Begin-Colin, *ACS Applied Nano Materials* **2018**, *1*, 4306.

[13] G. Cotin, F. Perton, C. Petit, S. Sall, C. Kiefer, V. Begin, B. Pichon, C. Lefevre, D. Mertz, J.-M. Greneche, S. Begin-Colin, *Chem. Mater.* **2020**, *32*, 9245.

[14] L. M. Bronstein, X. Huang, J. Retrum, A. Schmucker, M. Pink, B. D. Stein, B. Dragnea, *Chemistry of Materials* **2007**, *19*, 3624.

[15] B. H. Kim, K. Shin, S. G. Kwon, Y. Jang, H.-S. Lee, H. Lee, S. W. Jun, J. Lee, S. Y. Han, Y.-H. Yim, D.-H. Kim, T. Hyeon, *Journal of the American Chemical Society* **2013**, *135*, 2407.

[16] A. Lassenberger, T. A. Grünewald, P. D. J. van Oostrum, H. Rennhofer, H. Amenitsch, R. Zirbs, H. C. Lichtenegger, E. Reimhult, *Chem. Mater.* **2017**, *29*, 4511.

[17] F. Perton, G. Cotin, C. Kiefer, J.-M. Strub, S. Cianferani, J.-M. Greneche, N. Parizel, B. Heinrich, B. Pichon, D. Mertz, S. Begin-Colin, *Inorg. Chem.* **2021**, *60*, 12445.

[18] H. F. Drake, G. S. Day, S. W. Vali, Z. Xiao, S. Banerjee, J. Li, E. A. Joseph, J. E. Kuszynski, Z. T. Perry, A. Kirchon, O. K. Ozdemir, P. A. Lindahl, H.-C. Zhou, *Chem. Commun.* **2019**, *55*, 12769.

[19] P. N. Nelson, R. A. Taylor, *Applied Petrochemical Research* **2014**, *4*, 253.

[20] A. Skoulios, D. Guillon, *Molecular Crystals and Liquid Crystals Incorporating Nonlinear Optics* **1988**, *165*, 317.

[21] H. Abied, D. Guillon, A. Skoulios, P. Weber, A. M. Giroud-godquin, J. C. Marchon, *Liquid Crystals* **1987**, *2*, 269.

[22] A. M. Giroud-Godquin, J. C. Marchon, D. Guillon, A. Skoulios, *J. Phys. Chem.* **1986**, *90*, 5502.

[23] P. Maldivi, D. Guillon, A.-M. Giroud-Godquin, J.-C. Marchon, H. Abied, H. Dexpert, A. Skoukios, *J. Chim. Phys.* **1989**, *86*, 1651.

[24] S. Pu, C. Gong, A. W. Robertson, *R. Soc. open sci.* **2020**, *7*, 191204.

[25] A. S. Kashin, V. P. Ananikov, *Nat Rev Chem* **2019**, *3*, 624.

[26] J. J. De Yoreo, S. N. A. J. M., *Nat Rev Mater* **2016**, *1*, 16035.

[27] N. de Jonge, F. M. Ross, *Nature Nanotech* **2011**, *6*, 695.

[28] F. M. Ross, Ed. , *Liquid Cell Electron Microscopy*, Cambridge University Press, **2016**.

[29] N. Ortiz Peña, D. Ihiawakrim, M. Han, B. Lassalle-Kaiser, S. Carenco, C. Sanchez, C. Laberty-Robert, D. Portehault, O. Ersen, *ACS Nano* **2019**, *13*, 11372.

[30] J. J. De Yoreo, *Progress in Crystal Growth and Characterization of Materials* **2016**, *62*, 69.

[31] N. T. K. Thanh, N. Maclean, S. Mahiddine, *Chem. Rev.* **2014**, *114*, 7610.

[32] T. J. Woehl, J. E. Evans, I. Arslan, W. D. Ristenpart, N. D. Browning, *ACS Nano* **2012**, *6*, 8599.

[33] K. L. Jungjohann, S. Bliznakov, P. W. Sutter, E. A. Stach, E. A. Sutter, *Nano Lett.* **2013**, *13*, 2964.

[34] J. Baumgartner, A. Dey, P. H. H. Bomans, C. Le Coadou, P. Fratzl, N. A. J. M. Sommerdijk, D. Faivre, *Nature Mater* **2013**, *12*, 310.
[35] U. Mirsaidov, J. P. Patterson, H. Zheng, *MRS Bull.* **2020**, *45*, 704.
[36] Y. Zhang, D. Keller, M. D. Rossell, R. Erni, *Chem. Mater.* **2017**, *29*, 10518.
[37] T. J. Woehl, T. Moser, J. E. Evans, F. M. Ross, *MRS Bull.* **2020**, *45*, 746.
[38] N. M. Schneider, M. M. Norton, B. J. Mendel, J. M. Grogan, F. M. Ross, H. H. Bau, *J. Phys. Chem. C* **2014**, *118*, 22373.
[39] T. J. Woehl, P. Abellan, *Journal of Microscopy* **2017**, *265*, 135.
[40] N. Bhattarai, D. L. Woodall, J. E. Boercker, J. G. Tischler, T. H. Brintlinger, *Nanoscale* **2019**, *11*, 14573.
[41] J. Cookman, V. Hamilton, L. S. Price, S. R. Hall, U. Bangert, *Nanoscale* **2020**, *12*, 4636.
[42] C. de Gracia Lux, B. Donnio, B. Heinrich, M. P. Krafft, *Langmuir* **2013**, *29*, 5325.
[43] E. B. Sirota, H. E. King, D. M. Singer, H. H. Shao, *The Journal of Chemical Physics* **1993**, *98*, 5809.
[44] F. Perton, **2019**.
[45] H. Chang, B. H. Kim, H. Y. Jeong, J. H. Moon, M. Park, K. Shin, S. I. Chae, J. Lee, T. Kang, B. K. Choi, J. Yang, M. S. Bootharaju, H. Song, S. H. An, K. M. Park, J. Y. Oh, H. Lee, M. S. Kim, J. Park, T. Hyeon, *J. Am. Chem. Soc.* **2019**, *141*, 7037.
[46] A. Feld, A. Weimer, A. Kornowski, N. Winckelmans, J.-P. Merkl, H. Kloust, R. Zierold, C. Schmidtke, T. Schotten, M. Riedner, S. Bals, H. Weller, *ACS Nano* **2019**, *13*, 152.
[47] W. Baaziz, B. P. Pichon, S. Fleutot, Y. Liu, C. Lefevre, J.-M. Greneche, M. Toumi, T. Mhiri, S. Begin-Colin, *J. Phys. Chem. C* **2014**, *118*, 3795.
[48] K. Morigaki, P. Walde, *Langmuir* **2002**, *18*, 10509.
[49] M. Delample, F. Jérôme, J. Barrault, J.-P. Douliez, *Green Chem.* **2011**, *13*, 64.
[50] S.-H. Tung, H.-Y. Lee, S. R. Raghavan, *J. Am. Chem. Soc.* **2008**, *130*, 8813.
[51] J. M. Grogan, N. M. Schneider, F. M. Ross, H. H. Bau, *Nano Lett.* **2014**, *14*, 359.
[52] F. Kiss, J. Teplý, *International Journal for Radiation Physics and Chemistry* **1971**, *3*, 503.
[53] K.-S. Kim, J.-M. Lee, H.-Y. Seo, J.-H. Kim, H.-P. Song, M.-W. Byun, J.-H. Kwon, *Radiation Physics and Chemistry* **2004**, *71*, 47.
[54] S. K. P. Velu, M. Yan, K.-P. Tseng, K.-T. Wong, D. M. Bassani, P. Terech, *Macromolecules* **2013**, *46*, 1591.
[55] W. Baaziz, B. P. Pichon, Y. Liu, J.-M. Grenèche, C. Ulhaq-Bouillet, E. Terrier, N. Bergeard, V. Halté, C. Boeglin, F. Choueikani, M. Toumi, T. Mhiri, S. Begin-Colin, *Chemistry of Materials* **2014**, *26*, 5063.
[56] L. E. De-León-Prado, D. A. Cortés-Hernández, J. M. Almanza-Robles, J. C. Escobedo-Bocardo, J. Sánchez, P. Y. Reyes-Rdz, R. A. Jasso-Terán, G. F. Hurtado-López, *Journal of Magnetism and Magnetic Materials* **2017**, *427*, 230.
[57] D. Peddis, N. Yaacoub, M. Ferretti, A. Martinelli, G. Piccaluga, A. Musinu, C. Cannas, G. Navarra, J. M. Greneche, D. Fiorani, *Journal of Physics: Condensed Matter* **2011**, *23*, 426004.
[58] A. E. Deatsch, B. A. Evans, *Journal of Magnetism and Magnetic Materials* **2014**, *354*, 163.
[59] W. Baaziz, L. Truong-Phuoc, C. Duong-Viet, G. Melinte, I. Janowska, V. Papaefthimiou, O. Ersen, S. Zafeiratos, D. Begin, S. Begin-Colin, C. Pham-Huu, *J. Mater. Chem. A* **2014**, *2*, 2690.
[60] X. Liu, I. Marangon, G. Melinte, C. Wilhelm, C. Ménard-Moyon, B. P. Pichon, O. Ersen, K. Aubertin, W. Baaziz, C. Pham-Huu, S. Bégin-Colin, A. Bianco, F. Gazeau, D. Bégin, *ACS Nano* **2014**, *8*, 11290.
[61] G. Melinte, I. Florea, S. Moldovan, I. Janowska, W. Baaziz, R. Arenal, A. Wisnet, C. Scheu, S. Begin-Colin, D. Begin, C. Pham-Huu, O. Ersen, *Nat Commun* **2014**, *5*, 4109.
[62] F. M. Ross, *Science* **2015**, *350*, aaa9886.